

Multigrid Approach to Incompressible Viscous Cavity Flows

William A. Wood,*

NASA Langley Research Center, Hampton, VA 23681

Two-dimensional incompressible viscous driven-cavity flows are computed for Reynolds numbers on the range 100–20,000 using a loosely coupled, implicit, second-order centrally-differenced scheme. Mesh sequencing and three-level V-cycle multigrid error smoothing are incorporated into the symmetric Gauss-Seidel time-integration algorithm. Parametrics on the numerical parameters are performed, achieving reductions in solution times by more than 60 percent with the full multigrid approach. Details of the circulation patterns are investigated in cavities of 2-to-1, 1-to-1, and 1-to-2 depth to width ratios.

Nomenclature

A	coefficients of linear system
B, B'	intermediate source terms
b	source term of linear system
C	continuity equation error
e, e'	error vectors
f	vector of dependent variables
g	source-term vector
\bar{g}	discretized form of g
h	depth of cavity
l	width of cavity
P	relative pressure
Re_e	Reynolds number, $\rho U l / \mu$
r, r'	residual vectors
s	arc-length fraction
s_1	grid-clustering parameter
t	time
U	speed of upper (driving) surface
u, v	cartesian velocities
x, y	cartesian coordinates
β	grid-clustering strength, $\beta > 1$
ϵ	convergence tolerance
ζ	vorticity
λ_x	$\Delta t / 2\Delta x$
λ_y	$\Delta t / 2\Delta y$
μ	viscosity
ρ	density (constant for incompressible flow)
σ_x	$\Delta t / Re_e \Delta x^2$
σ_y	$\Delta t / Re_e \Delta y^2$
ψ	stream function

Subscripts:

i	discrete indicie in x -direction; $i = 1, \dots, I$
j	discrete indicie in y -direction; $j = 1, \dots, J$
c, f, m	coarse, fine, and medium meshes
t, x, y	differentiation <i>w.r.t.</i> independent variables

Superscripts:

k	sub-iteration counter
n	time level

All quantities are non-dimensional. The reference values are $l, U, \rho U^2$, and U/l for lengths, velocities, pressure, and time, respectively. When subscripts are omitted, they are assumed to be at (i, j) .

Introduction

VISCOUS fluid flow in the driven cavity has long been a popular test case for evaluating numerical techniques. The problem statement is straightforward, the geometry simple, yet the governing equations are a non-linear system of partial differential equations whose stiffness can be adjusted via the Reynolds number, with higher Reynolds numbers applying increasing degrees of numerical difficulty in achieving a converged steady-state solution.

Recent investigations into this problem by Huser and Biringen¹ indicate that by a Reynolds number of 30,000 the flow has become fully unsteady, *ie* continuously evolving in time. Shen² reports a high-resolution scheme that predicts bifurcation of the cavity flow solution at Reynolds numbers as low as 10,000. Goodrich *et al*³ also find a periodic solution of this Hopf bifurcation.

*Aerospace Technologist, Aerothermodynamics Branch, Gas Dynamics Division.

A partial multigrid scheme has been applied to the problem by Nishida and Nobuyuki⁴ whereby the pressure equation was solved with a multigrid procedure and the momentum equations are advanced using a Runge-Kutta explicit scheme. Another recent solution on the square cavity have been put forth by Semeraro⁵ using the theta scheme.

The driven-cavity problem statement whose solution is sought with the present method was put forward by Rubin *et al.*⁶ A loosely-coupled implicit procedure is formulated based on symmetric Gauss-Seidel relaxation, incorporating three-level multigrid error smoothing on each of the governing equations to accelerate convergence.

Governing Equations

Incompressible flow is defined by the continuity equation with constant density,

$$u_x + v_y = 0 \quad (1)$$

in cartesian coordinates. The corresponding perfect-gas Navier-Stokes equations^{7, 8} can be written for the primitive variables, in non-conservative form, as,

$$u_t + uu_x + vv_y = -P_x + \frac{1}{R_e} \nabla^2 u \quad (2)$$

and,

$$v_t + uv_x + vv_y = -P_y + \frac{1}{R_e} \nabla^2 v \quad (3)$$

where the Laplacian operator is,

$$\nabla^2 = \frac{\partial^2}{\partial x^2} + \frac{\partial^2}{\partial y^2}$$

Differentiating (Eqns. 2, 3) and incorporating (Eqn. 1) yields the Poisson equation for the pressure, following Hoffmann,⁹ as,

$$\nabla^2 P = -C_t - (u_x^2 + 2u_y v_x + v_y^2) + \frac{1}{R_e} \nabla^2 C \quad (4)$$

where,

$$C = u_x + v_y$$

is the error of the continuity equation (Eqn. 1), which goes to zero in the converged solution.

Alternatively, the governing equations can be formulated for the vorticity and stream function.⁶ The vorticity equation of motion is,

$$\zeta_t + u\zeta_x + v\zeta_y = \frac{1}{R_e} \nabla^2 \zeta \quad (5)$$

and the Poisson equation for the stream function is,

$$\nabla^2 \psi = \zeta \quad (6)$$

The vorticity is related to the velocity components as,

$$\zeta = u_y - v_x$$

and the stream function by,

$$\psi_y = u, \quad \psi_x = -v$$

Discretization

The governing equations (Eqns. 2-6) are discretized using a first-order implicit formulation in time and second-order expressions for all spatial derivatives. Whether applying the governing equations in primitive-variable or stream-function/vorticity formulations, the equations take on two basic forms. Setting

$$f = [u, v, \zeta, P, \psi]^T \quad (7)$$

to represent the dependent variables in (Eqns. 2-6), we can write for the first three components of (Eqn. 7),

$$f_t + uf_x + vf_y - \frac{1}{R_e} \nabla^2 f = -g \quad (8)$$

and for the last two components of (Eqn. 7),

$$-\nabla^2 f = -g \quad (9)$$

where,

$$g = [P_x, P_y, 0, g_4, \zeta]^T$$

and,

$$-g_4 = C_t + u_x^2 + 2u_y v_x + v_y^2 - \frac{1}{R_e} \nabla^2 C$$

The discretization strategy will evaluate the components of f implicitly at the advanced timestep, while the nonlinear left-hand-side (LHS) terms u and v , as well as the right-hand side (RHS), g , are lagged at the previous timestep, creating a loosely-coupled set of equations. To reduce notation, f is used to represent f^{n+1} in the difference equations that follow.

Discretizing (Eqns. 8, 9) yields,

$$\begin{aligned} \frac{f - f^n}{\Delta t} + \frac{u^n}{2\Delta x} (f_{i+1} - f_{i-1}) + \frac{v^n}{2\Delta y} (f_{j+1} - f_{j-1}) \\ - \frac{1}{R_e \Delta x^2} (f_{i+1} - 2f + f_{i-1}) \\ - \frac{1}{R_e \Delta y^2} (f_{j+1} - 2f + f_{j-1}) = -\bar{g} \end{aligned} \quad (10)$$

and,

$$\begin{aligned} -\frac{1}{\Delta x^2} (f_{i+1} - 2f + f_{i-1}) - \frac{1}{\Delta y^2} (f_{j+1} - 2f + f_{j-1}) \\ = -\bar{g} \end{aligned} \quad (11)$$

The RHS \bar{g} is the discrete form of g ,

$$\bar{g} = \begin{bmatrix} \frac{P_{i+1}^n - P_{i-1}^n}{2\Delta x} \\ \frac{P_{j+1}^n - P_{j-1}^n}{2\Delta y} \\ 0 \\ \bar{g}_A \\ \zeta^n \end{bmatrix}$$

with,

$$\begin{aligned} -\bar{g}_A = & -\frac{C^n}{\Delta t} + \frac{(u_{i+1}^n - u_{i-1}^n)^2}{4\Delta x^2} + \\ & \frac{(u_{j+1}^n - u_{j-1}^n)(v_{i+1}^n - v_{i-1}^n)}{2\Delta x \Delta y} + \frac{(v_{j+1}^n - v_{j-1}^n)^2}{4\Delta y^2} - \\ & \frac{1}{Re} \left[\frac{C_{i+1}^n - 2C^n + C_{i-1}^n}{\Delta x^2} + \frac{C_{j+1}^n - 2C^n + C_{j-1}^n}{\Delta y^2} \right] \end{aligned}$$

and,

$$\begin{aligned} C^{n+1} &= 0, \\ C^n &= \frac{u_{i+1}^n - u_{i-1}^n}{2\Delta x} + \frac{v_{j+1}^n - v_{j-1}^n}{2\Delta y} \end{aligned}$$

The system of (Eqns. 10, 11) can be rearranged as,

$$\begin{aligned} A_{ij}f + A_{i+1}f_{i+1} + A_{i-1}f_{i-1} + \\ A_{j+1}f_{j+1} + A_{j-1}f_{j-1} = B_{ij} \end{aligned} \quad (12)$$

When solving for u , v , or ζ , the coefficients and RHS of (Eqn. 12) are defined as,

$$\begin{aligned} A_{ij} &= 1 + 2\sigma_x + 2\sigma_y \\ A_{i\pm 1} &= -\sigma_x \pm \lambda_x u^n, \quad A_{j\pm 1} = -\sigma_y \pm \lambda_y v^n \\ B_{ij} &= f^n - \Delta t \bar{g} \end{aligned}$$

using the notation,

$$\begin{aligned} \lambda_x &= \frac{\Delta t}{2\Delta x}, \quad \lambda_y = \frac{\Delta t}{2\Delta y} \\ \sigma_x &= \frac{\Delta t}{Re\Delta x^2}, \quad \sigma_y = \frac{\Delta t}{Re\Delta y^2} \end{aligned}$$

When solving the Poisson equations for P or ψ , the coefficients and RHS of (Eqn. 12) are defined as,

$$\begin{aligned} A_{ij} &= \frac{2}{\Delta x^2} + \frac{2}{\Delta y^2}, \quad B_{ij} = -\bar{g} \\ A_{i\pm 1} &= -\frac{1}{\Delta x^2}, \quad A_{j\pm 1} = -\frac{1}{\Delta y^2} \end{aligned}$$

Finally, the linearized system of governing equations (Eqn. 12) is written for interior points as,

$$Af = b, \quad i = [2, I-1], \quad j = [2, J-1] \quad (13)$$

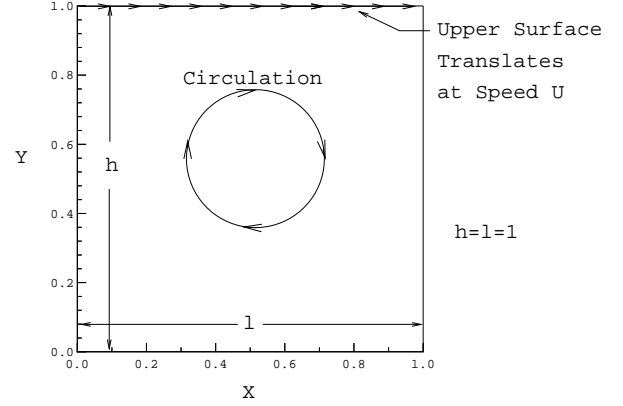


Fig. 1 Physical domain of driven cavity.

where the RHS is,

$$b = B + B'$$

and B' is used to move the boundary points from the LHS to the RHS,

$$B'_{i,j} = \begin{cases} -A_{i-1}f_{i-1}, & i = 2 \\ -A_{i+1}f_{i+1}, & i = I-1 \\ -A_{j-1}f_{j-1}, & j = 2 \\ -A_{j+1}f_{j+1}, & j = J-1 \\ 0, & i = [3, I-2], j = [3, J-2] \end{cases}$$

Thus, (Eqn. 13) is the linear system to be solved at each timestep to update the dependent variables from time level $t = n\Delta t$ to $t = (n+1)\Delta t$. This process is repeated until the steady-state solution is achieved.

Domain

The domain is a rectangular cavity of width l and depth h , oriented with the lower corner at the origin. An infinite upper surface is translated to the right with speed U . Figure 1 sketches the physical domain, indicating the anticipated flow circulation direction, clockwise, for positive U .

The domain is discretized on a structured cartesian grid. Two options for setting the grid-point spacing are available; uniform spacing or clustered to walls. The wall-clustering function used to generate the arclength fraction along $i=const$ or $j=const$ lines is,

$$s = \frac{s_1(\beta+1) - (\beta-1)}{2(s_1+1)}$$

where,

$$s_1 = \left(\frac{\beta+1}{\beta-1} \right)^{\frac{2i-(I+1)}{I-1}}$$

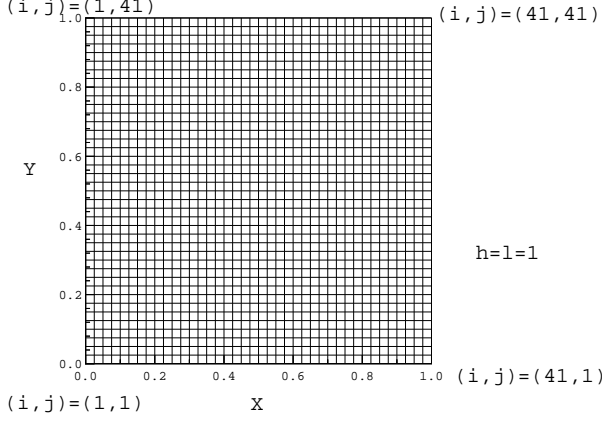


Fig. 2 Medium-level uniform mesh, 41 by 41 points.

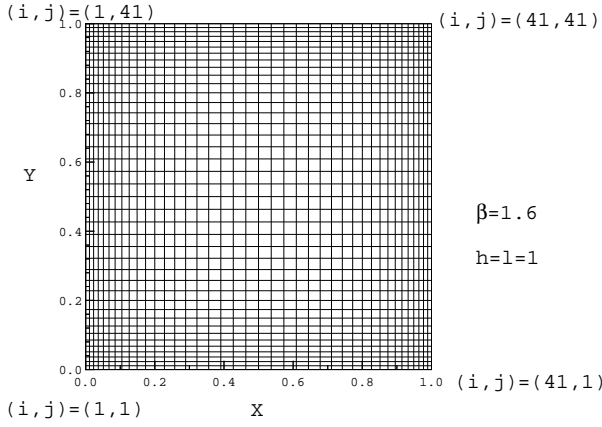


Fig. 3 Medium-level clustered mesh, 41 by 41 points.

The typical three-level multigrid procedure employed here solves the governing equations on an 81 by 81 fine-mesh and smoothes the error on two additional meshes, dimensioned 41 by 41 and 21 by 21, generated from the fine mesh by recursively removing every-other point. Sample 41 by 41 medium-coarseness meshes, which reproduce clearer than the fine meshes, are presented in Figure 2 for a uniform grid and Figure 3 for a grid clustered with $\beta = 1.6$. The 81 by 81 fine mesh can be inferred from Figures 2 and 3 by simply doubling the number of grid lines in both i and j directions.

Boundary and Initial Conditions

Viscous, solid walls are imposed on all four sides of the cavity. This imposes a no-slip condition on the velocity components at the wall. For pressure, the wall-normal pressure gradient is set to zero. This is the boundary-layer assumption, which becomes more accurate as the Reynolds number increases. The stream function is set to zero on the boundary.

On the left ($i = 1$) wall the conditions are expressed as,

$$u^{n+1} = v^{n+1} = 0$$

and,

$$P_x = 0 \Rightarrow P^{n+1} = \frac{4}{3}P_{i+1}^n - \frac{1}{3}P_{i+2}^n$$

for a second-order extrapolation, or for a first-order expression,

$$P_x = 0 \Rightarrow P^{n+1} = P_{i+1}^n$$

For the stream function and vorticity,

$$\psi^{n+1} = 0$$

$$\psi_x = 0 \Rightarrow \psi_{i-1}^n = \psi_{i+1}^n$$

$$\zeta = \psi_{xx} \Rightarrow \zeta^{n+1} = \frac{2}{\Delta x^2} \psi_{i+1}^n$$

Similarly, on the right ($i = I$) wall,

$$u^{n+1} = v^{n+1} = 0$$

$$P_x = 0 \Rightarrow P^{n+1} = \frac{4}{3}P_{i-1}^n - \frac{1}{3}P_{i-2}^n$$

$$\text{or, } P^{n+1} = P_{i+1}^n$$

$$\psi^{n+1} = 0$$

$$\psi_x = 0 \Rightarrow \psi_{i+1}^n = \psi_{i-1}^n$$

$$\zeta = \psi_{xx} \Rightarrow \zeta^{n+1} = \frac{2}{\Delta x^2} \psi_{i-1}^n$$

On the bottom ($j = 1$) wall,

$$u^{n+1} = v^{n+1} = 0$$

$$P_y = 0 \Rightarrow P^{n+1} = \frac{4}{3}P_{j+1}^n - \frac{1}{3}P_{j+2}^n$$

$$\text{or, } P^{n+1} = P_{j+1}^n$$

$$\psi^{n+1} = 0$$

$$\psi_y = 0 \Rightarrow \psi_{j-1}^n = \psi_{j+1}^n$$

$$\zeta = \psi_{yy} \Rightarrow \zeta^{n+1} = \frac{2}{\Delta y^2} \psi_{j+1}^n$$

The top ($j = J$) wall is translating horizontally, so,

$$u^{n+1} = U, \quad v^{n+1} = 0$$

$$P_y = 0 \Rightarrow P^{n+1} = \frac{4}{3}P_{j-1}^n - \frac{1}{3}P_{j-2}^n$$

$$\text{or, } P^{n+1} = P_{j-1}^n$$

$$\psi^{n+1} = 0$$

$$\psi_y = U \Rightarrow \psi_{j+1}^n = 2U\Delta y + \psi_{j-1}^n$$

$$\zeta = \psi_{yy} \Rightarrow \zeta^{n+1} = \frac{2}{\Delta y^2} (U\Delta y + \psi_{j-1}^n)$$

The boundary conditions are updated explicitly at each timestep.

The flowfield is initially at rest at $t = 0^-$, with all dependent variables set to zero, except for the pressure which is set to one everywhere. The upper boundary is then impulsively started at $t = 0^+$ to its full speed, U . Thus, the solution is started with the upper surface set to $u = U$ or $\zeta = 2U/\Delta y$.

Solution Procedure

Evolution in Time

Beginning with the initial conditions at time $t = 0^+$, the penta-diagonal linear system (Eqn. 13) is approximately inverted at each time step to advance the dependent variables to their steady-state values. This inversion is performed in a loosely-coupled fashion by iterating for the first, second, and then fourth components of (Eqn. 7) at each timestep when solving the primitive-variables formulation, or iterating for the third and then fifth components of (Eqn. 7) when solving the stream-function/vorticity formulation. Coupling between the equations is achieved when the A matrix and b vector of (Eqn. 13) are reformulated at each new time level.

Local time stepping is employed by setting Δt at each point to its maximum allowable value based on the input constraints on the two stability parameters λ_{max} and σ_{max} , such that,

$$\Delta t_{ij} = \min \left(\begin{array}{l} 2\lambda_{max} \cdot \min(\Delta x_{ij}, \Delta y_{ij}) \\ R_e \sigma_{max} \cdot \min((\Delta x_{ij})^2, (\Delta y_{ij})^2) \end{array} \right)$$

Local time stepping reduces the time accuracy of the solution on non-uniform meshes but is commonly employed to speed convergence to a steady-state result. The present algorithm already suffers poor time accuracy due to the first-order temporal derivative, lagged coefficients, loose coupling between governing equations, and approximate inversion of the linear system at each timestep. However, it is the steady-state solution that the present method seeks, whose accuracy is determined by the second-order formulation of the spatial derivatives, and not the time-history of the flow.

Relaxation Algorithm

A symmetric Gauss-Seidel (SGS) iteration sweep is performed to approximately invert $Af = b$. Forward and backward sub-iteration sweeps are performed for each component of f before moving on to the next component. This involves f_1 , f_2 , and f_4 for the primitive-variable formulation, or f_3 and f_5 for the stream-function/vorticity formulation. The forward sweep loops on i for each j ,

while the backward sweep loops on j for each i , attempting to minimize any bias in the solution from the SGS sweep directions.

A forward half-sweep of the SGS procedure on (Eqn. 12) at the k^{th} sub-iteration is,

$$f^{(k)} = \frac{1}{A_{ij}} \left(B_{ij} - A_{i+1}f_{i+1}^{(k-1)} - A_{i-1}f_{i-1}^{(k)} - A_{j+1}f_{j+1}^{(k-1)} - A_{j-1}f_{j-1}^{(k)} \right)$$

The backward portion of the symmetric sweep follows the same pattern as the forward sweep, but using the k^{th} values of the $i + 1$ and $j + 1$ variables. Typically, good performance is achieved with only 1–4 sub-iterations.

Grid Sequencing

Grid sequencing, or nested iterations, is employed at the beginning of the solution to speed convergence on the finest grid. The initial, coarsest grid is obtained from the fine mesh by retaining only every fourth point in both the i and j directions, for a factor of 16 reduction in the total number of grid points. The initial conditions are advanced on this grid for a number of timesteps equal to $I_c \cdot J_c / 2$.

The coarse-mesh solution is then prolonged to the medium mesh, which retains every-other grid point from the fine mesh. The prolongation employed here is a direct injection for overlapping points and two-point or four-point averaging for the interstitial points. Four times as many timesteps are then taken on the medium mesh as on the coarse mesh, and the resulting solution is then prolonged to the fine mesh, completing the grid sequencing.

Multigrid Cycle

A full three-level multigrid V -cycle is employed to damp low frequency errors in the solution. SGS relaxation on the fine mesh effectively damps the high frequency error content, but poorly damps low frequency errors.¹⁰ The multigrid cycle damps these low frequency errors by restricting the residual to progressively coarser meshes, aliasing the low frequencies to higher frequencies which are then damped effectively by the SGS relaxation algorithm. The error is then prolonged back to the fine-mesh solution as a correction to the dependent variables.

The three-level V -cycle begins by evolving the solution in time on the finest grid for a number of timesteps, typically 5–10. Then the residual is formed as,

$$r_f = b - Af$$

The residual is restricted, *via* simple point-to-point extraction, to the medium mesh, where the error equation

is relaxed,

$$Ae_m = r_m \quad (14)$$

A new residual is formed for this error equation as,

$$r'_m = r_m - Ae_m$$

and is restricted to the coarse mesh, where another error equation is relaxed,

$$Ae_c = r'_c$$

Once the error on the coarse mesh has been smoothed through several SGS sweeps the error e_c is prolonged to e'_m on the medium mesh, and is applied as a correction to e_m ,

$$e_m \leftarrow e_m + e'_m$$

Again the error is smoothed on the medium mesh (Eqn. 14) for several SGS sweeps and then the error e_m is prolonged back to e'_f on the fine mesh. The solution is now corrected by this error,

$$f \leftarrow f + e'_f$$

and is evolved in time again on the fine mesh for several timesteps. The multigrid cycle is then repeated until convergence is achieved for the fine-mesh solution.

Convergence Criteria

The L_2 -norm of the change in the dependent vector, f , between time-levels n and $n + 1$ is monitored to judge convergence,

$$\|f^{n+1} - f^n\|_2 < \epsilon$$

L_2 -norms are normalized by their value at the first timestep, with a typical value for ϵ of 10^{-4} .

Results

Test Case

A standard test case is chosen to compare the computational performance of the various techniques employed in the present method. Table 1 lists the parameters which are desired to be optimized using the test case.

The test case is chosen on the unit cavity, $h = l = 1$, with a uniform 81 by 81 fine mesh. The upper surface is translated to the right at speed $U = 1$, and the Reynolds number is 1000. The stream-function/vorticity form of the governing equations are solved.

Straight SGS relaxation without mesh sequencing or multigrid was used to generate the baseline solutions and optimize the maximum allowable timestep. For this case the timestep limit on Δt from λ_{max} is about six

Table 1 Algorithmic parameters to optimize.

Parameter	Test Values
$\lambda_{max}, \sigma_{max}$	1, 2, 3, 4
SGS sub-iterations	1, 2
Mesh sequencing	none, $\max(I, J)$, I+J, $I \cdot J/2$, $I \cdot J/4$, $I \cdot J/8$
V-cycle iteration pattern	none, $3_f-2_m-1_c-2_m-3_f$, $6_f-4_m-3_c-4_m-6_f$, $2_f-3_m-4_c-3_m-2_f$
Grid refinement	41×41 , 81×81

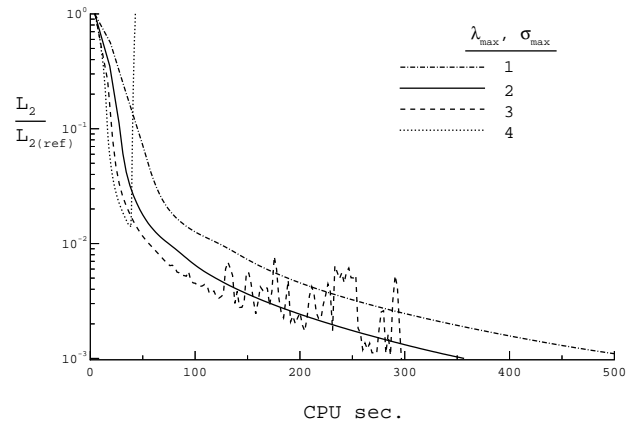


Fig. 4 Convergence rates for $\lambda_{max}, \sigma_{max}$ variations.

times more restrictive than from σ_{max} . Figure 4 compares convergence rates for various values of λ_{max} and σ_{max} . With $\lambda_{max} = 4$ the scheme is unstable, diverging after 50 timesteps. With a $\lambda_{max} = 3$, the solution does not diverge, but is clearly on the ragged edge of stability. Converging three orders of magnitude in 357 CPU seconds, $\lambda_{max} = 2$ gives the best convergence rate while maintaining stability, and is used for the remainder of the study. For smaller values of λ_{max} the convergence rate slows. Convergence rates, measured in CPU seconds, were obtained on a 40 MHz SUN Sparcstation 2 for the present study. Single-precision numerics, approximately seven significant digits, was used.

Figure 5 compares the effect of performing multiple SGS sweeps during each timestep. Performing two sets of forward and backward sweeps during each SGS cycle is seen to take longer to reach the converged steady-state solution, 400 *versus* 357 CPU seconds, than taking single forward-backward sweeps in each SGS cycle. With two SGS sweeps, $\lambda_{max} = 2$ proved to be unstable, so $\lambda_{max} = 1.5$ was used. This correspondingly smaller timestep is contributing to the two-pass SGS relaxation taking longer to converge.

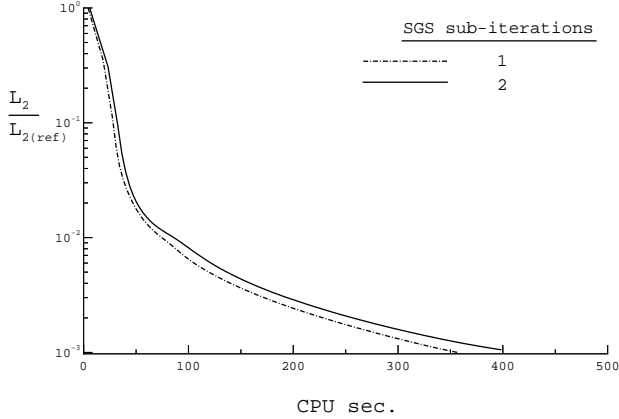


Fig. 5 Convergence using one and two SGS sub-iterations.

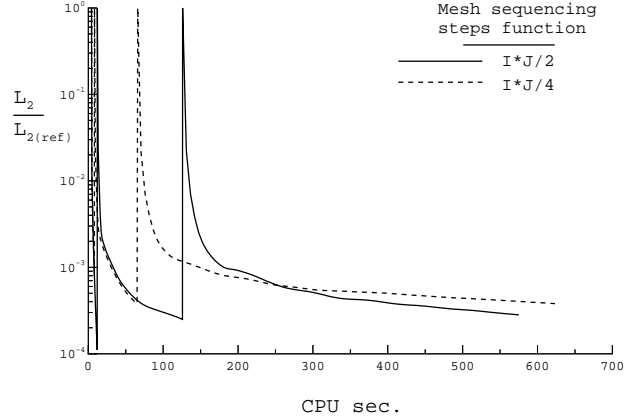


Fig. 7 Mesh sequencing convergence rates.

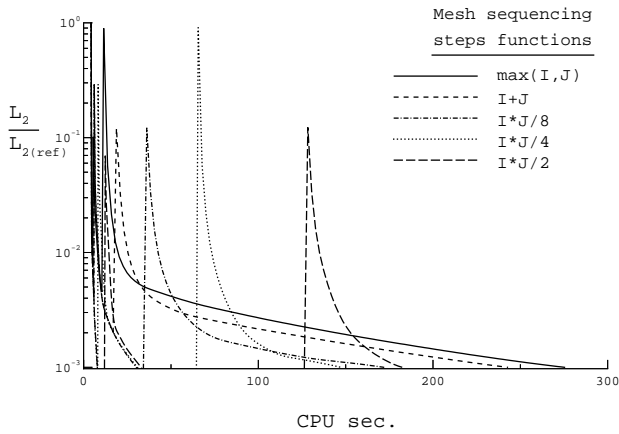


Fig. 6 Convergence rates with mesh sequencing.

Adding mesh sequencing to the solution procedure reduced the convergence time in half, to 147 CPU seconds. Several methods for specifying the number of coarse-grid iterations to perform were tested, and are listed in Table 1. The corresponding convergence rates are presented in Figure 6, where the general trend is that the more iterations taken on the coarser grids, the faster the overall convergence. Setting the convergence limit as $\epsilon = 10^{-3}$, the fastest convergence is obtained using,

$$\frac{I_c \cdot J_c}{4} = \frac{I \cdot J}{64}$$

steps on the coarse grid. The L_2 -norm jumps when the solution is prolonged to the medium mesh, where,

$$\frac{I_m \cdot J_m}{4} = \frac{I \cdot J}{16}$$

steps were taken before prolongating to the fine mesh. Similar trends are seen for the other functions used to

determine the number of steps to take on the nested grids.

While Figure 6 indicates the $I \cdot J/4$ function gives the fastest convergence in CPU time, the function $I \cdot J/2$ has a steeper convergence slope at $\epsilon = 10^{-3}$. Carrying these two functional variations to further convergence, Figure 7, shows that the functional form $I \cdot J/2$ converges the fastest toward $\epsilon = 10^{-4}$, and is the chosen function for the present method.

While mesh sequencing was found to speed convergence on the fine mesh, Figure 7 shows that the asymptotic convergence rate to small ϵ is still fairly slow. Adding multigrid to the solution procedure increases the rate of convergence to small ϵ by more effectively damping all frequency contents in the error. This change in the slope of convergence toward small ϵ using the multigrid approach is demonstrated in Figure 8, where all three variations in V -cycles for the multigrid implementation converge to $\epsilon = 10^{-4}$ in 450–500 CPU seconds, while the non-multigrid solution has reached an asymptotic convergence rate that will take at least twice as long to converge to $\epsilon = 10^{-4}$. The convergence histories of the multigrid solutions display spikes each time the error is prolonged back to the fine grid as a correction. While these correction steps temporarily increase the L_2 -norm, they clearly increase the global rate of convergence. All three V -cycles tested performed nearly the same, with the $3_f-2_m-1_c-2_m-3_f$ pattern performing the best, converging four orders of magnitude in 466 CPU seconds, and is the pattern chosen for the present method.

The velocity vectors for this cavity flow problem, as computed with the fastest-converging multigrid solution, are drawn in Figure 9. For clarity, only every fourth vector in both i and j directions has been plotted. The highest velocities are seen on the upper, driving surface, as expected. A strong circulation region forms on the interior of the cavity at this Reynolds number,

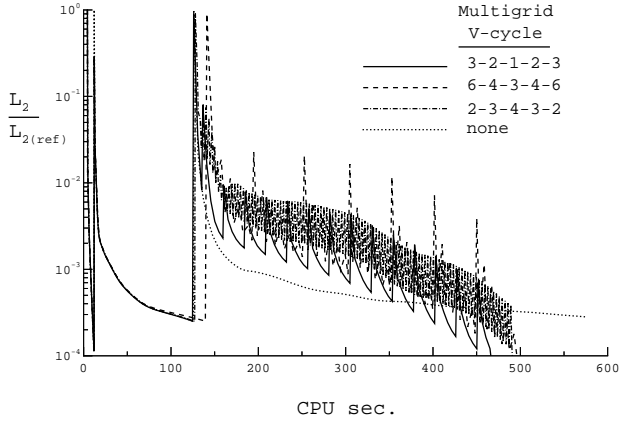


Fig. 8 Multigrid convergence rates with variations in V-cycle.

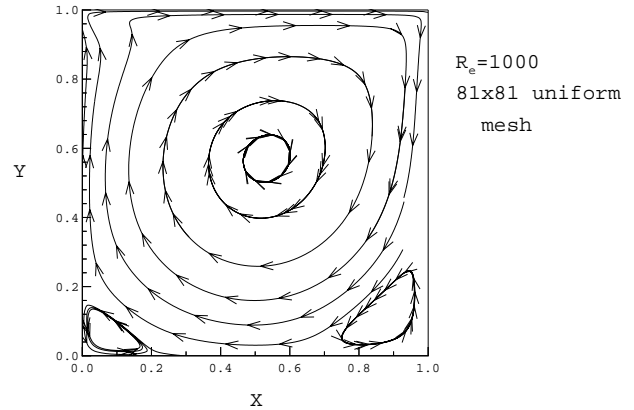


Fig. 10 Streamlines in viscous driven cavity.

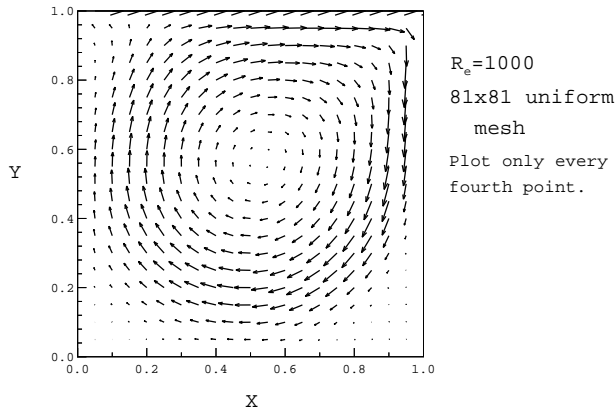


Fig. 9 Velocity vectors in viscous driven cavity.

$Re = 10^3$. The circulation resembles a solid-core rotation, with the highest velocities on the perimeter and decreasing velocities toward the center, as opposed to a vortex, which would have increasing velocities toward the eye. The bottom corners are regions of relatively stagnant flow, and the upper left corner shows the suction characteristic of the entrainment into the upper, driven boundary layer.

Figure 10 traces the corresponding streamlines. The primary circulation is seen to encompass nearly the entire cavity. Two recirculation regions are formed in each of the lower corners, but, recalling Figure 9, the velocity magnitudes are small in these recirculation regions.

Velocity components through the boundary layers are extracted in figure 11. The u component has been extracted along a vertical slice through the center of the domain while the v component is taken along a horizontal slice, again through the center of the domain. The central circulation region is confirmed to resemble a

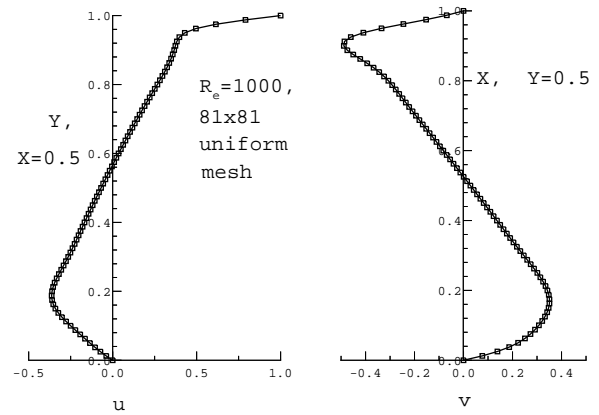


Fig. 11 Velocity component profiles through the core.

solid-core rotation, with linear velocity profiles through the core. Considering the grid-point distribution, the interior of the domain is well resolved. The bottom and left-wall boundary layers each have 15 points through the layer, providing moderate resolution. The upper surface and right wall have only 8–9 points through the laminar boundary layer.

Grid Convergence

The test case is repeated, on a uniform 41 by 41 mesh. Velocity components through the cavity are plotted in Figure 12, along with the 81 by 81-mesh solution from Figure 11. The 41 by 41 mesh is clearly not resolving the boundary-layer gradients nor the maximum velocities on the periphery of the circulation region. The linear trend in velocity variation through the circulation is picked up on the coarser grid. Since the 41 by 41-mesh solution does not generate the correct maximum velocities in the circulation, nor have the correct slope of the velocity profiles near the walls, and hence an inaccurate skin friction, the solution is not grid converged for this

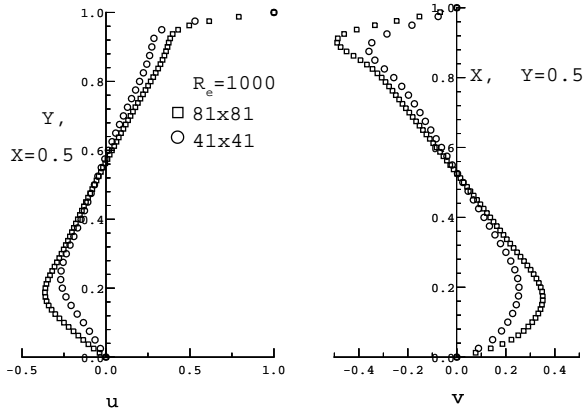


Fig. 12 Coarse-grid solution to viscous-cavity test case.

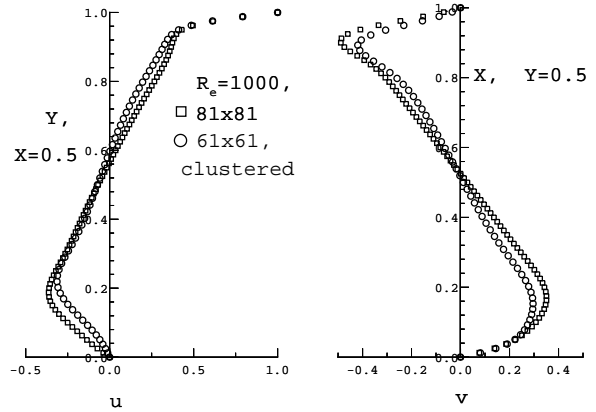


Fig. 14 Clustered-grid velocity profiles.

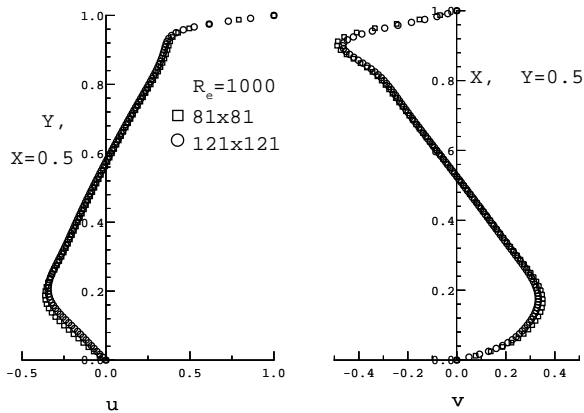


Fig. 13 Grid convergence for driven-cavity flow.

mesh.

The test case is repeated again, now on a 121 by 121 mesh. Figure 13 over-plots this very-fine mesh on the 81 by 81 solution. Excellent agreement is seen in the velocity profiles across the cavity. The boundary-layer profiles show good agreement as well on all walls, suggesting the 81 by 81-point mesh sufficiently resolves the flow at this Reynolds number.

Grid Clustering

The presence of the high velocity gradients in the boundary layers, as compared to the gradients on the interior of the cavity, suggests the use of a stretched grid to resolve the flow with fewer points, and hence in less time and computer resources.

Figure 14 over-plots the u and v velocity profiles across the cavity for the 81 by 81 uniform grid and a 61 by 61 clustered mesh. Both solutions are at a Reynolds number of 1000, and the clustered grid was

generated with $\beta = 1.6$. The basic flow pattern remains the same with the clustered grid, with good agreement through the upper boundary layer and across the primary circulation zone. However, the agreement is not as good in the bottom boundary layer and at the periphery of the circulation region, where the velocity peaks are under-predicted.

Better agreement is sought in the grid-clustered solutions, but the general trend of a degradation in the solution in the presence of stretching between mesh lines was seen in other cases as well. Sources of this error could arise from the single-precision numerics, the formulation of the algorithm for solving the governing equations, or in an unlocated programming bug. The inability to achieve reliable solutions with grid-point clustering to the walls limits the practical Reynolds number to which the present method can be applied.

High-Reynolds-Number Flows

Driven flow in the unit cavity at a Reynolds number of 2000 was computed on a 101 by 101 mesh. Cavity streamlines are drawn for this case in Figure 15. The streamline pattern for this case remains materially the same as for the $Re = 1000$ solution in Figure 10. Velocity profiles for $Re = 1000$ and $Re = 2000$ are plotted in Figure 16 at every fourth (i, j) point. The linearity in the velocity profiles through the circulation region is beginning to be lost at the higher Reynolds number and the boundary layers have thinned, but overall the flow has remained much the same with a doubling in Reynolds number.

Further increasing the Reynolds number to 5000 produces a dramatic shift in the flowfield. Figure 17 plots Velocity vectors for this case. Clearly, the primary central circulation has broken down, and is replaced by a clockwise circulation in the upper right corner and a counterclockwise recirculation of comparable

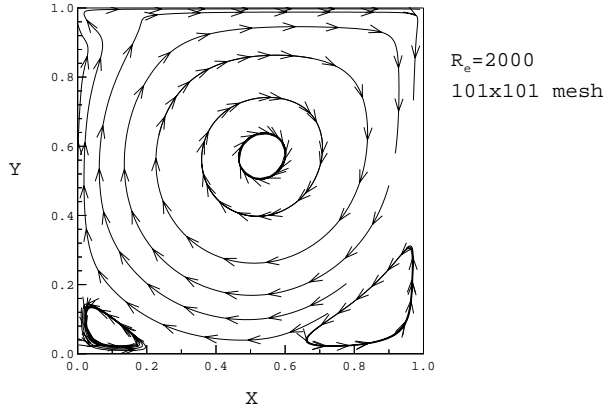


Fig. 15 Higher Reynolds number streamlines.

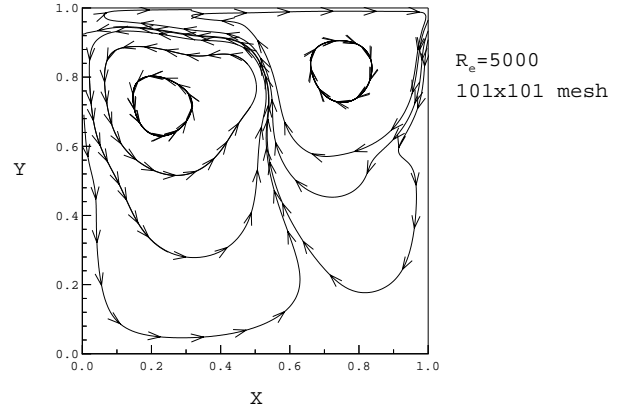


Fig. 18 Streamlines at $R_e = 5000$.

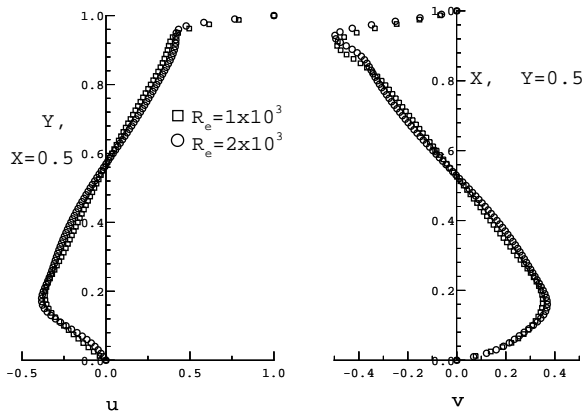


Fig. 16 Velocity profiles at higher Reynolds number.

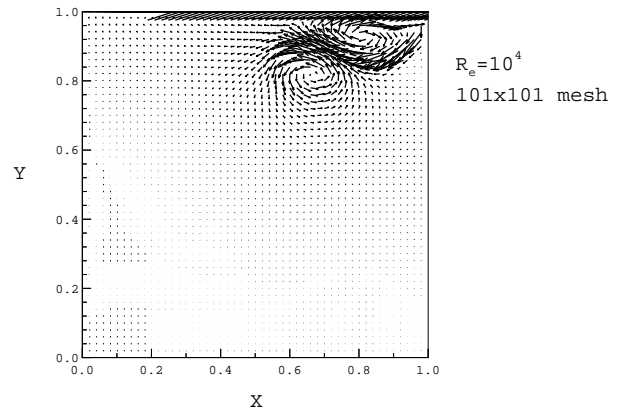


Fig. 19 Velocity vectors at $R_e = 10,000$.

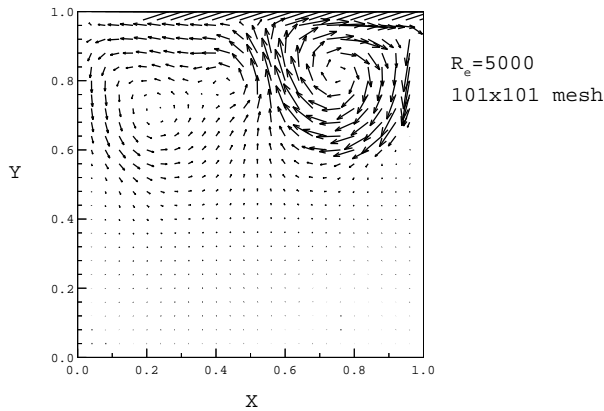


Fig. 17 Velocity vectors at $R_e = 5000$.

size, though of lower velocity magnitudes, near the upper left corner. The corresponding streamlines are traced in Figure 18, where the dual-circulation pattern is again observed.

Solutions were obtained as well for $R_e = 10,000$ and $R_e = 20,000$, the highest Reynolds number for which a reliable solution was obtainable in a reasonable amount of time, about one hour, with the present method. Velocity vectors for these two cases are plotted in Figures 19 and 20 at every-other (i, j) point. The circulation pattern seen at lower Reynolds numbers is breaking down, and the magnitude of velocities on the interior of the cavity are decreasing. The boundary layers are thinning as well, and are poorly resolved on the 101 by 101 mesh at $R_e = 20,000$.

The corresponding streamlines are traced in Figures 21 and 22. The primary circulation zone has continued to shrink in size in going from Reynolds numbers of 1000, to 5000, 10,000, and 20,000. Also, the counter-rotating recirculation has moved, from the upper-left corner at $R_e = 5000$, to a more central location at $R_e = 10,000$, and finally all the way to the upper-right corner by $R_e = 20,000$.

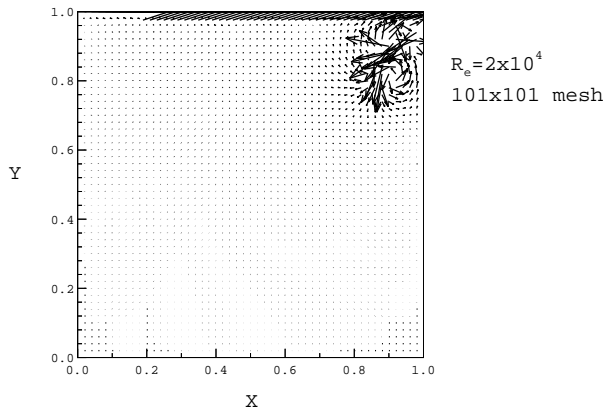


Fig. 20 Velocity vectors at $R_e = 20,000$.

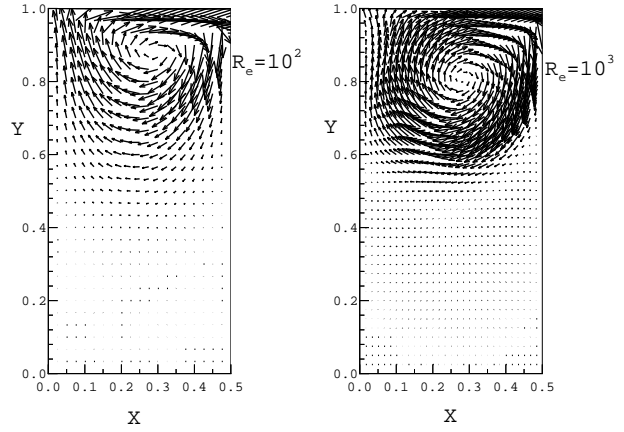


Fig. 23 Tall-cavity flows.

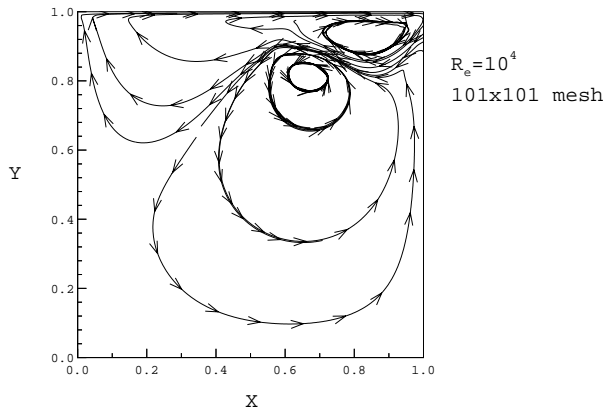


Fig. 21 Streamlines at $R_e = 10,000$.

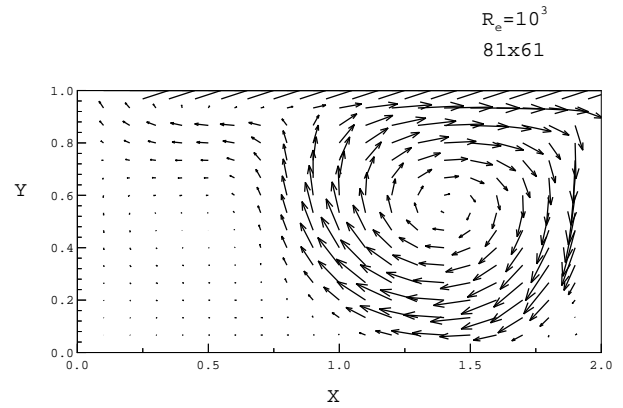


Fig. 24 Shallow-cavity velocity vectors.

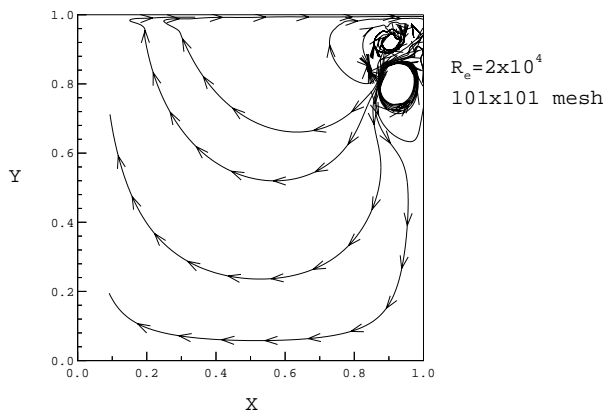


Fig. 22 Streamlines at $R_e = 20,000$.

Effect of Cavity Aspect Ratio

The cavity dimensions were changed so that the depth is twice the width. Solutions were generated at Reynolds numbers of 100 and 1000 on uniform 41 by 61 grids. Velocity vectors for these two cases are plotted in Figure 23. The circulation core is closer to the driving surface in the more viscous, $R_e = 100$, solution, while the higher Reynolds-number solution exhibits generally higher velocities around the circulation region.

The flowfield changes character when the cavity is made twice as wide as deep. Figure 24 plots velocity vectors, at every fourth (i, j) point, in a cavity with $h = 1$ and $l = 2$ at a Reynolds number of 1000. An 81 by 61 uniform mesh was used for this calculation. The strong primary circulation forms with a nearly circular shape at the right side of the cavity. The recirculation region on the left side of the cavity is approximately half the size of the primary circulation, though with much reduced velocities. Streamlines for this case are traced in Fig-

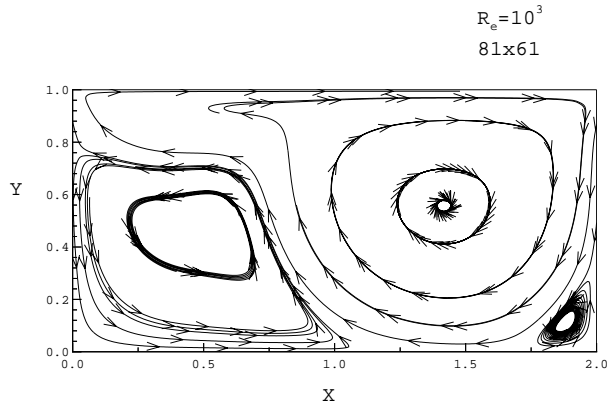


Fig. 25 Shallow-cavity streamlines.

ure 25, where a second, weak recirculation can be seen in the lower right corner.

Summary of Results

Incompressible viscous-flow solutions have been computed for the two-dimensional driven-cavity problem. The governing equations for perfect-fluid viscous flows have been discretized in a finite-difference formulation in a loosely coupled implicit scheme, formulated either in terms of the primitive variables or the stream-function and vorticity. Mesh sequencing and full, three-level, multigrid error smoothing are incorporated to speed convergence of the symmetric Gauss-Seidel time-integration algorithm.

Convergence was found to be faster when using a single, rather than multiple, symmetric Gauss-Seidel sweep at each time level to approximately invert the linear system. Several mesh sequencing iteration functions were tried, and the best was able to reduce solution time by 58 percent over an un-sequenced solution. The addition of the multigrid procedure further accelerated convergence on fine meshes.

At a Reynolds number of 1000 the cavity flow is characterized by a large solid-core circulation, encompassing nearly the entire domain. Counter-rotating circulations are found in the lower corners of the cavity, but with small velocities. As the Reynolds number is increased, the primary circulation is driven toward the upper-right corner, with the recirculations moving up and across the cavity. The highest Reynolds-number flow computed was at 20,000.

Vertical stretching of the cavity was not found to alter the flow patterns significantly, while horizontal stretching of the cavity created a large recirculation region, at a Reynolds number of 1000, and a laterally stretched entrainment pattern.

References

- ¹A. Huser and S. Biringen, "Calculation of Two-Dimensional Shear-Driven Cavity Flows at High Reynolds Numbers," *International Journal for Numerical Methods in Fluids*, vol. 14, pp. 1087–1189, Apr. 1992.
- ²J. Shen, "Hopf Bifurcation of the Unsteady Regularized Driven Cavity Flow," *Journal of Computational Physics*, vol. 95, pp. 228–245, July 1991.
- ³J. W. Goodrich, K. Gustafson, and K. Halasi, "Hopf Bifurcation in the Driven Cavity," *Journal of Computational Physics*, vol. 90, pp. 219–261, Sept. 1990.
- ⁴H. Nishida and N. Satofuka, "Higher-Order Solutions of Square Driven Cavity Flow Using a Variable-Order Multi-Grid Method," *International Journal for Numerical Methods in Engineering*, vol. 34, pp. 637–653, Mar. 1992.
- ⁵B. D. Semeraro and A. Sameh, "Solution of the Navier-Stokes Equations for a Driven Cavity," NASA CR 188008, Mar. 1991.
- ⁶S. G. Rubin and J. E. Harris, "Incompressible Viscous Flow in a Driven Cavity," in *Numerical Studies of Incompressible Viscous Flow in a Driven Cavity*, no. SP-378, ch. 1, pp. 1–6, NASA, 1975.
- ⁷M. Navier, "Mémoire sur les lois du Mouvement des Fluides," *Mémoire de l'Académie des Sciences*, vol. 6, p. 389, 1827.
- ⁸G. G. Stokes, "On the Theories of the Internal Friction of Fluids in Motion," *Trans. Cambridge Philosophical Society*, vol. 8, pp. 227–319, 1849.
- ⁹K. A. Hoffmann and S. T. Chiang, *Computational Fluid Dynamics For Engineers—Volume I*. Engineering Education System, 1993.
- ¹⁰G. Golub and J. M. Ortega, *Scientific Computing: An Introduction with Parallel Computing*. Academic Press, Inc. 1993.